

Oxygen Reduction

Epoxy-rich Fe Single Atom Sites Boost Oxygen Reduction Electrocatalysis

Yufei Zhao⁺, Ziyang Shen⁺, Juanjuan Huo⁺, Xianjun Cao, Pengfei Ou, Junpeng Qu, Xinming Nie,^{*} Jinqiang Zhang,^{*} Minghong Wu,^{*} Guoxiu Wang, and Hao Liu^{*}

Abstract: Electrocatalysts for highly efficient oxygen reduction reaction (ORR) are crucial for energy conversion and storage devices. Single-atom catalysts with maximized metal utilization and altered electronic structure are the most promising alternatives to replace current benchmark precious metals. However, the atomic level understanding of the functional role for each species at the anchoring sites is still unclear and poorly elucidated. Herein, we report Fe single atom catalysts with the sulfur and oxygen functional groups near the atomically dispersed metal centers (Fe1/NSOC) for highly efficient ORR. The Fe1/NSOC delivers a half-wave potential of 0.92 V vs. RHE, which is much better than those of commercial Pt/C (0.88 V), Fe single atoms on N-doped carbon (Fe1/NC, 0.89 V) and most reported nonprecious metal catalysts. The spectroscopic measurements reveal that the presence of sulfur group induces the formation of epoxy groups near the FeN₄S₂ centers, which not only modulate the electronic structure of Fe single atoms but also participate the catalytic process to improve the kinetics. The density functional theory calculations demonstrate the existence of sulfur and epoxy group engineer the charges of Fe reactive center and facilitate the reductive release of OH* (rate-limiting step), thus boosting the overall oxygen reduction efficiency.

Introduction

The design and discovery of highly efficient and cost-effective oxygen reduction reaction (ORR) electrocatalysts are critical for the development of proton exchange membrane fuel cells (PEMFCs) and metal-air batteries, which are the representatives as renewable energy sources to

provide clean energy and high power.^[1–3] Single-atom catalysts (SACs) have been considered efficient ORR catalysts with maximized metal atom utilization and well-defined active centers for structure–activity relationship investigation.^[4–8] Especially, it has been demonstrated that the atomically dispersed Fe–N–C catalysts with the FeN_x species as active centers are promising low-cost alternatives to platinum (Pt)-based catalysts toward ORR.^[9–13] Massive efforts have been made to enhance the ORR activity of Fe–N–C catalysts since its discovery. A positive correlation has been demonstrated between the catalytic activity and active site density or the intrinsic activity of a single site. Nevertheless, the nature of the catalytic activity is still unclear and in-depth mechanistic understanding is urgently needed.

The intrinsic catalytic activity of FeN_x for ORR is highly related to the electronic structure of active sites, which can be achieved by atomic level regulation. Controlling the properties of carbon supports or the coordination environment of center metals can efficiently alter the electronic structures of the active sites, and thereby optimize the adsorption/desorption of ORR intermediates. In particular, the incorporation of heteroatoms, e.g., S, P, Cl, into the atomic structure result in modulated electronic structures and d-band centers of the active sites due to the different electronegativity of heteroatoms and C/N atoms.^[14–20] For instance, Fe single-atom catalysts on N, S co-doped carbon support, N and P/S dual-coordinated Fe atoms, S atoms on carbon substrates modified Fe_xC/Fe, as atomically dispersed metal active sites, have exhibited appealing ORR performance.^[21–23] The above studies suggested the heteroatoms directly coordinated or beyond the first coordinated shell can efficiently engineer the properties of the metal

[*] Dr. Y. Zhao,⁺ Z. Shen,⁺ Dr. J. Huo,⁺ Dr. X. Cao, J. Qu, Prof. M. Wu
 Joint International Laboratory on Environmental and Energy
 Frontier Materials, School of Environmental and Chemical Engineering,
 Shanghai University (China)
 E-mail: mhwo@shu.edu.cn

Dr. P. Ou, Dr. J. Zhang
 Department of Electrical and Computer Engineering, University of
 Toronto
 35 St George Street, Toronto, Ontario, M5S 1A4 (Canada)
 E-mail: Jinqiang.Zhang@uts.edu.au

Prof. X. Nie
 School of Physics and Electronic Engineering, Jiangsu Normal
 University
 Xuzhou, Jiangsu 221116 (China)
 E-mail: nxinming@jnsu.edu.cn

Dr. J. Zhang, Prof. G. Wang, Prof. H. Liu
 Centre for Clean Energy Technology, University of Technology
 Sydney
 Broadway, Sydney, NSW-2007 (Australia)
 E-mail: Hao.liu@uts.edu.au

[†] These authors contributed equally to this work.

© 2023 The Authors. Angewandte Chemie International Edition published by Wiley-VCH GmbH. This is an open access article under the terms of the Creative Commons Attribution Non-Commercial NoDerivs License, which permits use and distribution in any medium, provided the original work is properly cited, the use is non-commercial and no modifications or adaptations are made.

centers for superior catalytic activity.^[24,25] Recently, it has been also demonstrated that the oxygen groups, such as the epoxy group, near the atomically dispersed metal centers play a significant role in determining the selectivity and catalytic activity during ORR process.^[26–28] Except for the modification effect, these nonmetal atoms (e.g., C and N atoms) in SACs can also participate in the electrocatalysis process as additional active sites, which offers a promising strategy to further boost the catalytic activity.^[29] However, in-depth understanding the roles of these heteroatoms in SACs is still missing, and a systematic investigation is of great significance to investigate the catalytic mechanism at the atomic level, which will guide the design of efficient catalysts.

Herein, we present a comprehensive investigation of N–S and C–O–C engineered single-atom FeN₄ catalysts (Fe1/NSOC) for ORR by integrated experimental and theoretical approaches. The presence of S species induces the formation of oxygen functional groups (epoxy group) near the center metal single atoms, modulating the electronic structure of Fe atoms. Furthermore, the reversible cleavage of C–O–C bonds during the ORR process can efficiently lower the energy barrier by functioning as an anchor site for OH* intermediates. The obtained Fe1/NSOC have exhibited superior ORR catalytic activity of half-wave potentials of 0.92 V vs. RHE, stability and selectivity, exceeding the benchmark Pt/C catalysts and most of the reported state-of-the-art catalysts. Such high activity of Fe1/NSOC can be attributed to the Fe reactive center co-engineered by sulfur and epoxy groups, which is more favorable for the reductive release of OH* as demonstrated by density functional theory (DFT) calculations. This work provides an atomic-level understanding of the functional role of the species at the anchoring sites, which opens an avenue for designing high-performance catalysts.

Results and Discussion

The schematic illustration of the typical preparation route of Fe1/NSOC is shown in Figure 1a. The preparation is based on the hard template fabrication of SBA-15 (SEM image in Figure S1).^[30,31] The as-synthesized SBA-15 was introduced into the mixed solution of Fe precursor, thiourea and 1,10-phenanthroline at the temperature of 80 °C to form Fe-phenanthroline coated on the template. This pre-coordination strategy of Fe by phenanthroline resulted in the atomically dispersed Fe centers after high-temperature pyrolysis, template removal and acid treatment. Additionally, the existence of thiourea to form N–S species in the carbon substrate could also facilitate the formation of epoxy group (C–O–C) around single atom sites which further engineered the Fe active centers.

The scanning electron microscopy (SEM) and transmission electron microscopy (TEM) images of the Fe1/NSOC in Figure 1b–c and S2a demonstrate the inverse replicate of the rod-shaped framework of SBA-15, showing a highly ordered mesoporous structure. The high-resolution TEM images in Figure 1d and S2b demonstrated the ordered

channel of 3.5 nm and the partially graphitic properties of Fe1/NSOC. This is highly beneficial to the mass and electron transfer in the ORR process. No particles or clusters have been identified on the carbon matrix, suggesting the Fe species are atomically dispersed, further demonstrated by the high angle annular dark-field scanning transmission electron microscopy (HAADF-STEM) image of Fe1/NSOC in Figure 1e. A number of bright spots at the atomic range are spotted on the carbon support, referring to the atomically dispersed Fe atoms. The elemental mappings in Figure 1f and S3 disclose the homogeneous distribution of elements C, N, Fe, O, and S on the entire structure of Fe1/NSOC.

NSC and Fe1/NC comparative samples were synthesized for comparison through the same synthesis approach without adding metal precursor and S source, respectively. As shown in Figure S4–5, the SEM and TEM images of NSC and Fe1/NC show no discernible differences from those of Fe1/NSOC. The mapping results reveal the C, N, O, Fe or C, N, O, S homogeneous distributed properties. The above results demonstrated that the incorporation of Fe and S precursors has no effect on the achieved morphology and structure.

The N₂ adsorption-desorption isotherm results of Fe1/NSOC in Figure 1g show a large surface area of 1141 m²g^{−1}, which is higher than those of NSC (979 m²g^{−1}) and Fe1/NC (1058 m²g^{−1}). Moreover, the type IV isotherm curves (the inset of Figure 1g) present a clear hysteresis implying the presence of mesopores with a diameter of ≈3.3 nm, which is consistent with the TEM result (Figure 1d) and the wall thickness of SBA-15. The high surface area and mesopores in Fe1/NSOC lead to more exposed active sites and accelerated mass transportation, beneficial for the ORR process. Moreover, Fe1/NSOC exhibited higher Fe loading on the carbon matrix of 1.68 wt % compared to that of Fe1/NC (1.37 wt %) determined by inductively coupled plasma-mass spectrometry (ICP-MS), revealing that the S species could assist/stabilize the formation of Fe single atoms. The X-ray diffraction (XRD) patterns in Figure S6a show only two dominant peaks at around 24° and 44° for the three samples, attributing to the (002) and (101) planes of the graphitic carbon.^[32] It is noteworthy that no metal diffraction peaks are observed in the XRD patterns, suggesting the Fe species are atomically dispersed on the substrate without the formation of large nanoparticles. The Raman spectra of Fe1/NSOC, Fe1/NC and NSC in Figure S6b exhibit a typical D and G band at ≈1345 cm^{−1} and ≈1590 cm^{−1}, respectively, with the I_D/I_G values 0.945, 0.962 and 0.966, suggesting slightly higher graphitic properties of the carbon substrate has been achieved for Fe1/NSOC.^[33]

The chemical states of the as-prepared samples were further studied by X-ray photoelectron spectroscopic (XPS). The high-resolution XPS spectra of N 1s for Fe1/NSOC and Fe1/NC (Figure S7a) exhibit similar peak positions and intensities, suggesting the existence of pyridinic N/Fe–N, pyrrolic N and graphitic N.^[26,34] The presence of Fe–N indicates the Fe single atoms coordinated with the surrounding N atoms in both catalysts. The high-resolution O 1s XPS spectra in Figure 2a show the peaks for three oxygen

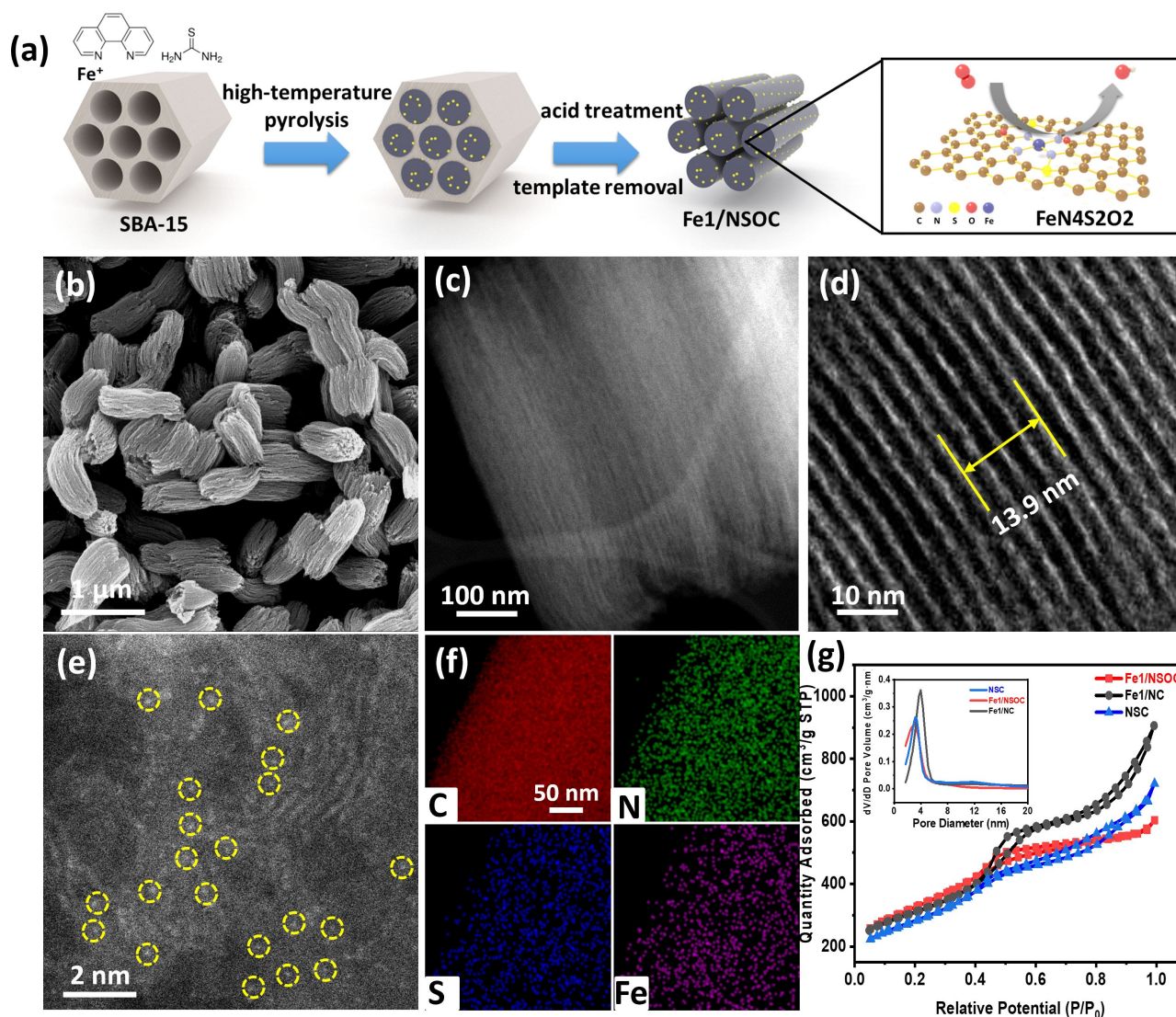


Figure 1. Preparation and morphology characterization of Fe1/NSOC. a) The schematic illustration for the preparation procedure of Fe1/NSOC. b–e) SEM, HAADF-STEM, high-resolution TEM and HAADF-STEM images of Fe1/NSOC. f) Elemental distribution of C, N, S, and Fe elements in Fe1/NSOC. g) Nitrogen adsorption/desorption isotherm of Fe1/NSOC, Fe1/NC and NSC.

components, including ketonic oxygen (C=O, O1, ≈ 531.2 eV), oxygen atoms in epoxy (C–O–C) or hydroxyl groups and carbonyl oxygen in ester groups (O2, ≈ 532.0 eV), and the epoxy oxygen in ester groups (O3, ≈ 533.2 eV).^[28] However, the percentage of epoxy oxygen atoms for Fe1/NSOC (60%) is obviously much higher than that in Fe1/NC (32.8%), demonstrating the epoxy groups dominate the oxygen species in Fe1/NSOC. Two dominant peaks located at 164.1 and 165.4 eV can be observed for the high-resolution S 2p of Fe1/NSOC, attributing to the S 2p_{3/2} and 2p_{1/2} of sulfide species (Figure S7b).^[35,36] The small peak at around 168.2 eV is ascribed to the sulfate species. The peak positions of Fe in Fe1/NSOC and Fe1/NC (Figure 2b) reveal that the Fe species appear at their oxidation states instead of metallic states. Moreover, a slight peak shift to higher binding energy can be observed from Fe1/NC to Fe1/NSOC, suggesting the oxidation states of Fe increased with

the S and O species engineering strategies. The chemical state and coordination environment of Fe species in Fe1/NSOC were further investigated by the X-ray absorption spectroscopy (XAS) measurements. Figure 2c shows the Fe K-edge X-ray absorption near-edge structure (XANES) curves of Fe1/NSOC and the reference samples of Fe foil, Fe₂O₃, iron phthalocyanine (FePc). It can be observed that the line position (absorption edge) of Fe–N/S–C is close to Fe₂O₃, indicating the valence states of Fe species are around Fe³⁺. The Fourier-transformed *k*³-weighted EXAFS (FT-EXAFS) spectra of Fe1/NSOC in Figure 2d and S8 show a prominent peak located at 1.46 Å, no peaks associated with Fe–Fe (at 2.2 Å) or Fe–S (at 1.8 Å) are observed, confirming the Fe species atomically dispersed and stabilized by surrounding N atoms. The wavelet transforms (WT) of the *k*³-weighted EXAFS spectra in Figure 2f show the structure information in both *k* and *R* spaces. The WT contour plots

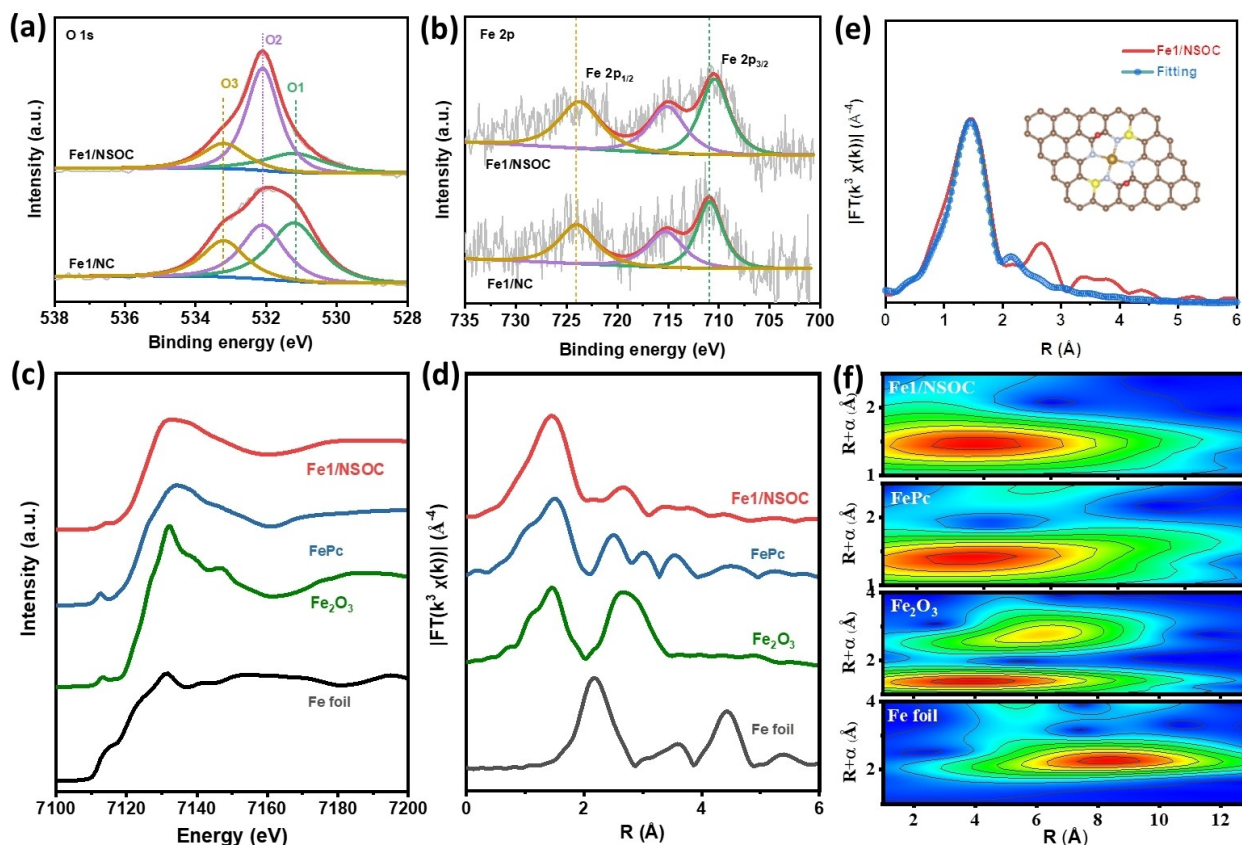


Figure 2. Structural characterizations of Fe1/NSOC. a, b) The high-resolution XPS spectra of O 2p and Fe 2p of Fe1/NSOC and Fe1/NC. c, d) The normalized XANES spectra and the k^3 -weighted Fourier transform of EXAFS spectra at Fe K-edge of Fe1/NSOC and the reference materials. e) EXAFS curves between the experimental data and the fit of Fe1/NSOC. The insets are the fitted structures. f) Wavelet transform for the k^3 -weighted EXAFS spectra of Fe1/NSOC and the reference materials.

of Fe1/NSOC display only one intensity between 4 and 5 Å, ascribing to the bonds of Fe-light atoms, which demonstrates the presence of atomically dispersed Fe species in Fe1/NSOC. The local coordination configuration of Fe species in Fe1/NSOC is further studied by the quantitative EXAFS fitting. The fitting results demonstrate the Fe-N₄ model matches well with Fe1/NSOC with a coordination number (CN) of 4.17 ± 0.23 (Figure 2e), which suggests that the Fe-N₄ are the main moieties in the as-prepared Fe1/NSOC.

The ORR measurements were conducted in O₂-saturated 0.1 M KOH media using the rotating disk electrode. The cyclic voltammetry (CV) curves of Fe1/NSOC, Fe1/NC and NSC in Figure S9 show no redox peaks in N₂-saturated KOH solution. In contrast, well-defined cathodic peaks appear for the three samples in O₂-saturated media, referring to their ORR catalytic capability. Moreover, the peak for Fe1/NSOC (0.841 V vs. RHE) is positively shifted compared to those of Fe1/NC (0.838 V vs. RHE) and NSC (0.769 V vs. RHE), implying the superior ORR performance of Fe1/NSOC. The ORR catalytic activities of the as-prepared materials were further evaluated by Linear sweep voltammetry (LSV). The catalytic activities of commercial 20 wt % Pt/C were also investigated as the reference. Fe1/NSOC exhibits superior ORR capability with an extremely high onset and half-wave potentials of 1.08 and 0.92 V vs.

RHE, respectively, and a limiting current density of 6.00 mA cm⁻² (Figure 3a–b), which is much better than Fe1/NC (1.06 V, 0.89 V), NSC (1.02 V, 0.86 V) and reference commercial Pt/C (1.02 V, 0.88 V). Such performance is also among the best of most up-to-date Fe single atoms-based ORR catalysts (Table S3). Meanwhile, the kinetic current density of Fe1/NSOC is 51.75 mA cm⁻² at 0.85 V vs. RHE, which is 2.0, 7.7 and 4.2 times superior to those of Fe1/NC (26.14 mA cm⁻²), NSC (6.73 mA cm⁻²) and commercial Pt/C (12.23 mA cm⁻²), respectively (Figure 3b). The Tafel slope of Fe1/NSOC presented in Figure S10 is 77 mV dec⁻¹, which is lower than those of Fe1/NC (90 mV dec⁻¹), NSC (100 mV dec⁻¹) and commercial Pt/C (89 mV dec⁻¹), demonstrating much faster ORR reaction kinetics of Fe1/NSOC. Fe1/NSOC also deliver a higher mass activity of 0.63 A mg⁻¹_{Fe} at the potential of 0.92 V vs. RHE compared to that of Fe1/NC (0.41 A mg⁻¹_{Fe}). Fe1/NSOC exhibited excellent ORR capability in the acidic condition of 0.1 M HClO₄ as well with a half-wave potential of 0.76 V vs. RHE and a limiting current density of 6.6 mA cm⁻² (Figure S11). Furthermore, Fe1/NSOC shows an increasing performance with the increase of rotating speed from 400 to 2025 rpm, indicating an enhanced O₂ diffusion for the ORR activity (Figure 3c). The calculated Koutechy–Levich (K–L) plots in Figure S12 show excellent linear and parallel characteristics,

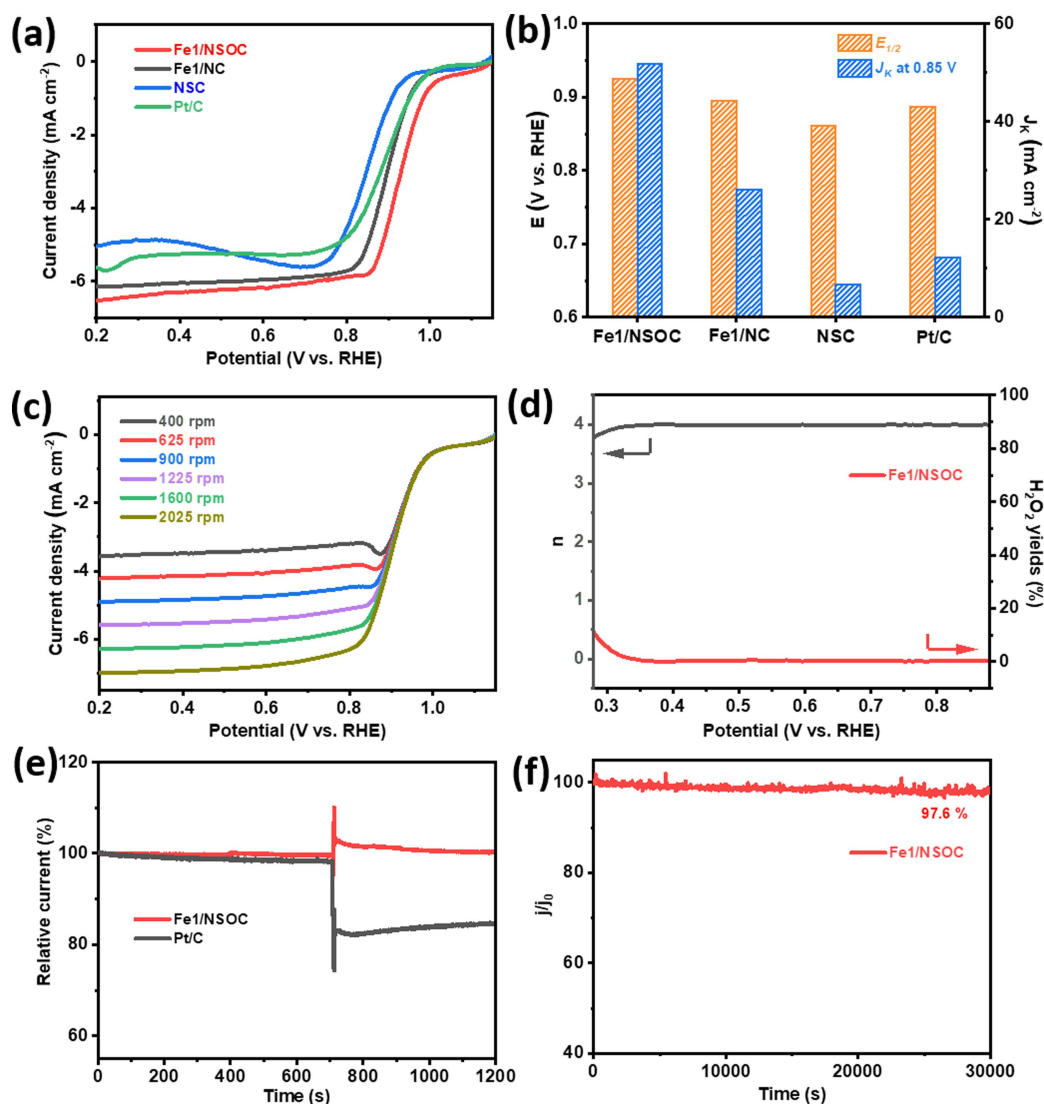


Figure 3. ORR catalytic performance of Fe1/NSOC. a) ORR polarization curves of Fe1/NSOC, Fe1/NC, NSC and Pt/C in O₂-saturated 0.1 M KOH solution with a rotation rate of 1600 rpm. b) The comparison of $E_{1/2}$ and J_k at 0.85 V of Fe1/NSOC, Fe1/NC, NSC and Pt/C. c) LSV curves of Fe1/NSOC at various rotation rates, d) electron transfer number and H₂O₂ yield of Fe1/NSOC and Pt/C. e) chronoamperometric curves of a methanol crossover test with Fe1/NSOC and Pt/C. f) Stability result for Fe1/NSOC.

elucidating Fe1/NSOC possesses first-order ORR reaction kinetics. Similar phenomena are also observed for Fe1/NC and NSC (Figure S13). Product selectivity was performed by rotating ring-disk electrode measurements that the electron-transfer numbers (n) and H₂O₂ yields were calculated (Figure 3d). In the potential range of 0.28 to 0.88 V, the n value is close to 4.0 and H₂O₂ yield is less than 10%, suggesting Fe1/NSOC catalysts possess a primary four-electron ORR pathway. In addition, Fe1/NSOC catalysts exhibit excellent resistance to methanol crossover with a slight change in the observed current after injecting 5% (v/v) methanol into the media (Figure 3e), whereas a significant decay occurs for the reference Pt/C, demonstrating the excellent methanol tolerance capability of Fe1/NSOC catalyst. The durability of Fe1/NSOC was assessed by the chronoamperometry measurement ($i-t$). The results in Figure 3f show that Fe1/NSOC maintain 97.6% current of the

initial after 30,000 s, indicating excellent stability in alkaline conditions. The TEM images in Figure S14 show no obvious structural change and clusters/particles aggregations are observed after the stability test, further confirming the outstanding stability of Fe1/NSOC during ORR process.

The superior catalytic activity of Fe1/NSOC over NSC suggests that the Fe species could be the active sites for oxygen reduction. The hypothesis was demonstrated by further evaluating the ORR performance of Fe1/NSOC in 0.1 M KOH solution containing 10 mM of KSCN, which is capable of binding with the metal species, thus lowering the corresponding catalytic activity during electrocatalysis.^[37,38] As shown in Figure S15, the ORR performance of Fe1/NSOC decreases after the incorporation of KSCN, with the $E_{1/2}$ negative shift of 40 mV. This reveals that the Fe single atom sites are the active sites for ORR, while the

surrounding environment (epoxy and S groups) helps to boost the performance (Figure 3a).

DFT calculations were further performed to identify the electronic structures of the active sites. Three atomic structures with sulfur and epoxy groups positioned at different positions (FeN4S2O2-1, FeN4S2O2-2, FeN4S2O2-3) have been constructed to investigate their influence (Figure 4a). It appears that both structures of FeN4S2O2-1 and FeN4S2O2-2 with N–S and C–O–C groups are stable (different positions of epoxy group), while the N–S and C–O–C in FeN4S2O2-3 tend to convert into N–S and S–O–C groups due to its relatively unstable nature. As shown in Figure 4b–c and S16–19, Fe1/NSOC with all three different configurations display the same rate-determining steps to those of Fe1/NC with FeN4 and Fe1/NSC with FeN4S2 atomic structure (the last step of *OH reduction), however, much lower limiting barriers have been achieved for Fe1/NSOC, demonstrating that the incorporation of sulfur and epoxy group can influence the electronic structure of center Fe single atoms, thus enhancing the catalytic capability. Furthermore, the atomic structure of FeN4S2O2-1 shows the lowest energy barrier among the three configurations of Fe1/NSOC for the OH-releasing processes (−0.79 eV for FeN4S2O2-1, −0.75 eV for FeN4S2O2-2, −0.66 eV for FeN4S2O2-3), indicating the position among N–S, C–O–C and Fe active centers also influence the ORR catalytic activity.

The detailed electronic structures of Fe1/NSOC have been explored to further elucidate the superior ORR catalytic activity. The charge density distributions in Figure 4d show the Fe center in FeN4S2O2-1 exhibited much

higher charge density compared to that of FeN4 due to the presence of S/O atoms, indicating the electron transfer from Fe single atom to the carbon substrate and resulting in the redistribution of Fe 3d-orbital electrons. This contributes to the boosted ORR catalytic activity and lower energy barrier of Fe1/NSOC.^[15,39] The projected density of states (PDOS) and the d-band center (ϵ_d) of Fe atoms in Fe1/NSOC and Fe1/NC have been calculated. The different PDOS results of active Fe atoms on FeN4S2O2-1 and FeN4 in Figure 4e may originate from the changing spin state of Fe orbital, which effectively boosts the charge transport and enhances the ORR process.^[40,41] Therefore, the existence of S/O atoms in Fe1/NSOC promotes the corresponding catalytic capability.

It has been established that the existence of epoxy group has positive effect on the ORR catalytic activity while the position of the epoxy group also plays an important role (Figure 4). To investigate their actual influence on the ORR performance, we further performed chemical treatments to alter the surface state and re-construct the surrounding environment. Specifically, Fe1/NSOC was chemically treated in the solutions containing either H₂O₂ (Fe1/NSOC-H₂O₂) or NaBH₄ (Fe1/NSOC-NaBH₄). The postmortem characterizations indicate that there is no obvious change in the XRD and Raman spectra compared to the original Fe1/NSOC, suggesting the oxidation and reduction have no effect on the aggregation of Fe species and carbon properties (Figure S20). Moreover, the high-resolution S 2p spectra in Figure 5a exhibit almost no change before and after oxidation and reduction treatment. However, the peaks for oxygen atoms in epoxy have been decreased obviously for both Fe1/NSOC-H₂O₂ and Fe1/NSOC-NaBH₄ after the

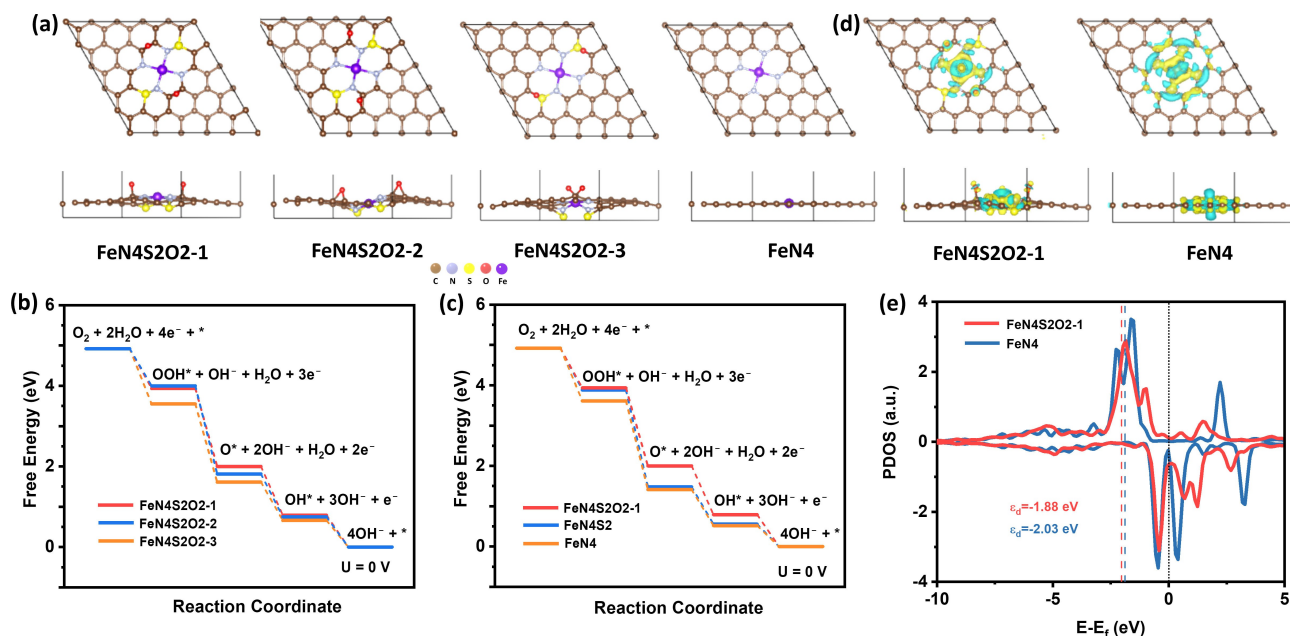


Figure 4. DFT calculation results of Fe1/NSOC. a) The top and side view of the atomic structure of FeN4S2O2-1, FeN4S2O2-2, FeN4S2O2-3 and FeN4. b, c) Free-energy paths of ORR intermediates on FeN4S2O2-1, FeN4S2O2-2, FeN4S2O2-3, FeN4S2 and FeN4. d) The top and side view of deformation electronic density of FeN4S2O2-1 and FeN4. The blue region represents charge depletion and the yellow region indicates charge accumulation; the isosurface value is 0.003 e/Bohr³. e) The PDOS of d orbitals of active Fe atoms on FeN4S2O2-1 and FeN4. The dotted black line for Fermi level, and the dashed line for d-band centers (ϵ_d).

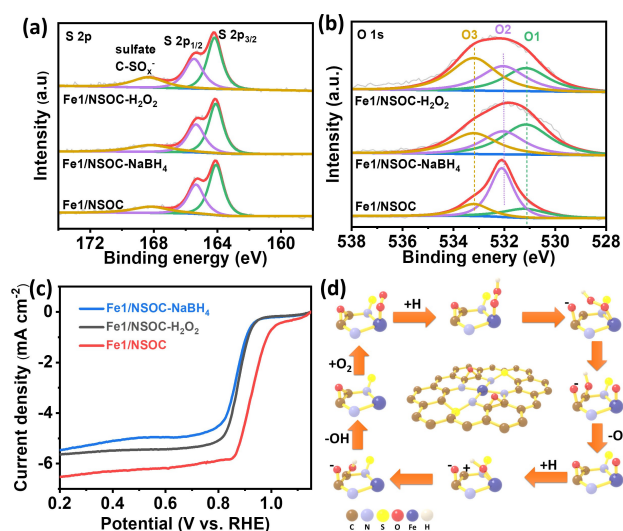


Figure 5. The investigation of epoxy groups boosting ORR performance. a, b) The high-resolution XPS spectra of S 2p and O 2p of Fe1/NSOC, Fe1/NSOC-H₂O₂ and Fe1/NSOC-NaBH₄. c) ORR polarization curves of Fe1/NSOC, Fe1/NSOC-H₂O₂ and Fe1/NSOC-NaBH₄. d) Mechanism illustration of epoxy groups participating in ORR process.

treatment, whereas the peak for ketonic oxygen (C=O, O1, ≈ 531.2 eV) and the epoxy oxygen in ester groups (O3, ≈ 533.2 eV) have been increased for Fe1/NSOC-NaBH₄ and Fe1/NSOC-H₂O₂, respectively (Figure 5b). As a result, the high-resolution Fe 2p spectra of Fe1/NSOC-H₂O₂ and Fe1/NSOC-NaBH₄ in Figure S21a exhibit a slight positive peak shift to higher binding energy compared to the original Fe1/NSOC. However, the electrochemical test results in Figure 5c show an obvious $E_{1/2}$ dropping from 0.92 V vs. RHE of Fe1/NSOC to 0.86 and 0.87 V vs. RHE of Fe1/NSOC-H₂O₂ and Fe1/NSOC-NaBH₄, respectively, which may suggest that the epoxy group plays additional roles in boosting the ORR. Since the similar structures (ketonic and ester groups) have no such boosting effect compared to the epoxy groups (Figure 5b), we assign it to the direct participation of epoxy groups in the ORR process in addition to the modulating of electronic structures of Fe single atoms (Figure 5d). We propose that one C–O bond in the epoxy group breaks during the reaction to form negatively charged O and positively charged C sites. The positively charged sites are prone to interact with O species/intermediates during the ORR process, functioning as an OH* anchoring site while facilitating the bond cleavage to accelerate the reaction, which should significantly reduce energy barriers of OH releasing processes (rate-determining step in DFT, Figure 4b and S22). The resulting vicinal diol structures quickly lose H₂O molecules to return to the epoxy group which will be ready for the next interaction again. Therefore, the existence of epoxy groups is highly beneficial to facilitate the overall ORR. This could also explain the best result of structure FeN₄S₂O₂-1 as it shows the most optimal distance between the epoxy group and Fe single atom sites.

Conclusion

We reported the sulfur and oxygen functional groups co-engineered Fe single atoms at the anchoring sites (Fe1/NSOC) as highly efficient catalysts for ORR. The presence of sulfur group induces the formation of epoxy group to further modulate the electronic structure of Fe single atoms. Fe1/NSOC have exhibited much superior ORR performance to Fe1/NC with no sulfur group and much lower epoxy group. The mechanism investigation (H₂O₂/NaBH₄ treatments) also confirms the significant role of the epoxy group in boosting the ORR performance of Fe1/NSOC. DFT calculations demonstrate the existence of sulfur and epoxy group highly modulate the charges of Fe center, making it more favorable for the reductive release of OH* and thus the promoted ORR performance. Furthermore, Fe1/NSOC is methanol tolerant and stable toward ORR (degradation of 2.4% in 0.1 M KOH solution). This work offers an innovative strategy to design atomically dispersed catalysts with the functional role of the species at the anchoring sites to boost the catalytic performance for energy conversion and storage systems.

Supporting Information

The authors have cited additional references within the Supporting Information.

Acknowledgements

All authors thank the support from the “Joint International Laboratory on Environmental and Energy Frontier Materials” and “Innovation Research Team of High-Level Local Universities in Shanghai”. H.L. thanks the financial support from Australian Research Council (FT180100705). Y. Z. acknowledges the support from the National Natural Science Foundation of China (22209103). J. Z. thanks the support from UTS Chancellor’s Research Fellowships. Open Access publishing facilitated by University of Technology Sydney, as part of the Wiley - University of Technology Sydney agreement via the Council of Australian University Librarians.

Conflict of Interest

The authors declare no conflict of interest.

Data Availability Statement

The data that support the findings of this study are available in the supplementary material of this article.

Keywords: Epoxy Group · Fe Reactive Center · Oxygen Reduction Reaction · Sulfur Group

- [1] A. Kulkarni, S. Siahrostami, A. Patel, J. K. Nørskov, *Chem. Rev.* **2018**, *118*, 2302–2312.
- [2] X. Huang, Z. Zhao, L. Cao, Y. Chen, E. Zhu, Z. Lin, M. Li, A. Yan, A. Zettl, Y. M. Wang, X. Duan, T. Mueller, Y. Huang, *Science* **2015**, *348*, 1230–1234.
- [3] Y. Zhao, J. Zhang, X. Guo, X. Cao, S. Wang, H. Liu, G. Wang, *Chem. Soc. Rev.* **2023**, *52*, 3215–3264.
- [4] M. Xiao, J. Zhu, G. Li, N. Li, S. Li, Z. P. Cano, L. Ma, P. Cui, P. Xu, G. Jiang, H. Jin, S. Wang, T. Wu, J. Lu, A. Yu, D. Su, Z. Chen, *Angew. Chem. Int. Ed.* **2019**, *58*, 9640–9645.
- [5] Y. Yang, Y. Yang, Z. Pei, K.-H. Wu, C. Tan, H. Wang, L. Wei, A. Mahmood, C. Yan, J. Dong, S. Zhao, Y. Chen, *Matter* **2020**, *3*, 1442–1476.
- [6] M. A. Hunter, J. M. T. A. Fischer, Q. Yuan, M. Hankel, D. J. Searles, *ACS Catal.* **2019**, *9*, 7660–7667.
- [7] J. Huo, Z. Shen, X. Cao, L. Li, Y. Zhao, H. Liu, G. Wang, *Small* **2022**, *18*, 2202394.
- [8] Z. Jiang, W. Sun, H. Shang, W. Chen, T. Sun, H. Li, J. Dong, J. Zhou, Z. Li, Y. Wang, R. Cao, R. Sarangi, Z. Yang, D. Wang, J. Zhang, Y. Li, *Energy Environ. Sci.* **2019**, *12*, 3508–3514.
- [9] L. Jiao, G. Wan, R. Zhang, H. Zhou, S.-H. Yu, H.-L. Jiang, *Angew. Chem. Int. Ed.* **2018**, *57*, 8525–8529.
- [10] K. Liu, J. Fu, Y. Lin, T. Luo, G. Ni, H. Li, Z. Lin, M. Liu, *Nat. Commun.* **2022**, *13*, 2075.
- [11] X. Xie, L. Peng, H. Yang, G. I. N. Waterhouse, L. Shang, T. Zhang, *Adv. Mater.* **2021**, *33*, 2101038.
- [12] C. Shu, Q. Tan, C. Deng, W. Du, Z. Gan, Y. Liu, C. Fan, H. Jin, W. Tang, X.-d. Yang, X. Yang, Y. Wu, *Carbon Energy* **2022**, *4*, 1–11.
- [13] H.-B. Zhang, Y. Meng, H. Zhong, L. Zhang, S. Ding, L. Fang, T. Li, Y. Mei, P.-X. Hou, C. Liu, S. P. Beckman, Y. Lin, H.-M. Cheng, J.-C. Li, *Carbon Energy* **2023**, *5*, e289.
- [14] L. Hu, C. Dai, L. Chen, Y. Zhu, Y. Hao, Q. Zhang, L. Gu, X. Feng, S. Yuan, L. Wang, B. Wang, *Angew. Chem. Int. Ed.* **2021**, *60*, 27324–27329.
- [15] J. Zhang, Y. Zhao, C. Chen, Y.-C. Huang, C.-L. Dong, C.-J. Chen, R.-S. Liu, C. Wang, K. Yan, Y. Li, G. Wang, *J. Am. Chem. Soc.* **2019**, *141*, 20118–20126.
- [16] Z. Chen, H. Niu, J. Ding, H. Liu, P.-H. Chen, Y.-H. Lu, Y.-R. Lu, W. Zuo, L. Han, Y. Guo, S.-F. Hung, Y. Zhai, *Angew. Chem. Int. Ed.* **2021**, *60*, 25404–25410.
- [17] L. Fan, X. Wei, X. Li, Z. Liu, M. Li, S. Liu, Z. Kang, F. Dai, X. Lu, D. Sun, *Nano Res.* **2023**, *16*, 1810–1819.
- [18] H. Shen, E. Gracia-Espino, J. Ma, K. Zang, J. Luo, L. Wang, S. Gao, X. Mamat, G. Hu, T. Wagberg, S. Guo, *Angew. Chem. Int. Ed.* **2017**, *56*, 13800–13804.
- [19] P. Chen, T. Zhou, L. Xing, K. Xu, Y. Tong, H. Xie, L. Zhang, W. Yan, W. Chu, C. Wu, Y. Xie, *Angew. Chem. Int. Ed.* **2017**, *56*, 610–614.
- [20] L. Peng, J. Yang, Y. Yang, F. Qian, Q. Wang, D. Sun-Waterhouse, L. Shang, T. Zhang, G. I. N. Waterhouse, *Adv. Mater.* **2022**, *34*, 2202544.
- [21] Q. Li, W. Chen, H. Xiao, Y. Gong, Z. Li, L. Zheng, X. Zheng, W. Yan, W.-C. Cheong, R. Shen, N. Fu, L. Gu, Z. Zhuang, C. Chen, D. Wang, Q. Peng, J. Li, Y. Li, *Adv. Mater.* **2018**, *30*, 1800588.
- [22] Y. Qiao, P. Yuan, Y. Hu, J. Zhang, S. Mu, J. Zhou, H. Li, H. Xia, J. He, Q. Xu, *Adv. Mater.* **2018**, *30*, 1804504.
- [23] Y. Chen, S. Ji, S. Zhao, W. Chen, J. Dong, W.-C. Cheong, R. Shen, X. Wen, L. Zheng, A. I. Rykov, S. Cai, H. Tang, Z. Zhuang, C. Chen, Q. Peng, D. Wang, Y. Li, *Nat. Commun.* **2018**, *9*, 5422.
- [24] Y. Zhao, W.-J. Jiang, J. Zhang, E. C. Lovell, R. Amal, Z. Han, X. Lu, *Adv. Mater.* **2021**, *33*, 2102801.
- [25] J. Zhang, H. Yang, B. Liu, *Adv. Energy Mater.* **2021**, *11*, 2002473.
- [26] J. Huo, X. Cao, Y. Tian, L. Li, J. Qu, Y. Xie, X. Nie, Y. Zhao, J. Zhang, H. Liu, *Nanoscale* **2023**, *15*, 5448–5457.
- [27] C. H. Choi, H.-K. Lim, M. W. Chung, G. Chon, N. Ranjbar Sahraie, A. Altin, M.-T. Sougrati, L. Stievano, H. S. Oh, E. S. Park, F. Luo, P. Strasser, G. Dražić, K. J. J. Mayrhofer, H. Kim, F. Jaouen, *Energy Environ. Sci.* **2018**, *11*, 3176–3182.
- [28] Q. Zhang, X. Tan, N. M. Bedford, Z. Han, L. Thomsen, S. Smith, R. Amal, X. Lu, *Nat. Commun.* **2020**, *11*, 4181.
- [29] H. Fei, J. Dong, Y. Feng, C. S. Allen, C. Wan, B. Voloskiy, M. Li, Z. Zhao, Y. Wang, H. Sun, P. An, W. Chen, Z. Guo, C. Lee, D. Chen, I. Shakir, M. Liu, T. Hu, Y. Li, A. I. Kirkland, X. Duan, Y. Huang, *Nat. Catal.* **2018**, *1*, 63–72.
- [30] P. Verma, Y. Kuwahara, K. Mori, R. Raja, H. Yamashita, *Nanoscale* **2020**, *12*, 11333–11363.
- [31] F. Gao, Q. Lu, D. Zhao, *Adv. Mater.* **2003**, *15*, 739–742.
- [32] M. B. Gawande, P. Fornasiero, R. Zbořil, *ACS Catal.* **2020**, *10*, 2231–2259.
- [33] J.-D. Yi, R. Xu, Q. Wu, T. Zhang, K.-T. Zang, J. Luo, Y.-L. Liang, Y.-B. Huang, R. Cao, *ACS Energy Lett.* **2018**, *3*, 883–889.
- [34] H. B. Yang, S.-F. Hung, S. Liu, K. Yuan, S. Miao, L. Zhang, X. Huang, H.-Y. Wang, W. Cai, R. Chen, J. Gao, X. Yang, W. Chen, Y. Huang, H. M. Chen, C. M. Li, T. Zhang, B. Liu, *Nat. Energy* **2018**, *3*, 140–147.
- [35] S. Chen, X. Li, C.-W. Kao, T. Luo, K. Chen, J. Fu, C. Ma, H. Li, M. Li, T.-S. Chan, M. Liu, *Angew. Chem. Int. Ed.* **2022**, *61*, e202206233.
- [36] W. Zhang, X. Guo, C. Li, J.-Y. Xue, W.-Y. Xu, Z. Niu, H. Gu, C. Redshaw, J.-P. Lang, *Carbon Energy* e317.
- [37] Y. Zhao, P. V. Kumar, X. Tan, X. Lu, X. Zhu, J. Jiang, J. Pan, S. Xi, H. Y. Yang, Z. Ma, T. Wan, D. Chu, W. Jiang, S. C. Smith, R. Amal, Z. Han, X. Lu, *Nat. Commun.* **2022**, *13*, 2430.
- [38] Y. Wang, A. Cho, G. Jia, X. Cui, J. Shin, I. Nam, K.-J. Noh, B. J. Park, R. Huang, J. W. Han, *Angew. Chem. Int. Ed.* **2023**, *62*, e202300119.
- [39] S. Wang, L. Zhang, Z. Xia, A. Roy, D. W. Chang, J.-B. Baek, L. Dai, *Angew. Chem. Int. Ed.* **2012**, *51*, 4209–4212.
- [40] F. Ando, T. Gunji, T. Tanabe, I. Fukano, H. D. Abruña, J. Wu, T. Ohsaka, F. Matsumoto, *ACS Catal.* **2021**, *11*, 9317–9332.
- [41] Z. Wang, J. Huang, L. Wang, Y. Liu, W. Liu, S. Zhao, Z.-Q. Liu, *Angew. Chem. Int. Ed.* **2022**, *61*, e20211469.

Manuscript received: June 13, 2023

Accepted manuscript online: July 15, 2023

Version of record online: July 27, 2023